Materials Advances

PAPER

View Article Online
View Journal | View Issue

Cite this: *Mater. Adv.*, 2024, 5, 8505

Open Access Article. Published on 24 September 2024. Downloaded on 2/13/2026 4:09:46 PM.
This article is licensed under a Creative Commons Attribution 3.0 Unported Licence.

Halogen substituted bithiophene-based polycatenars with tunable fluorescence†

Mohamed Alaasar, *[ab] Yu Cao, [cd] Thorben Neumann,[e] Tianyi Tan,[c] Feng Liu [c] and Michael Giese *[e]

Received 31st July 2024,
Accepted 22nd September 2024

DOI: 10.1039/d4ma00771a

rsc.li/materials-advances

Efficient synthesis of extended π-conjugated systems containing sulphur-rich aromatics is of special interest for organic electronics. Herein, we report the synthesis of new π-conjugated 5,5′-diphenyl-2,2′-bithiophene-based tricatenars. The materials have the same aromatic backbone ending at one terminus with a 3,5-diheptyloxy substituted-benzene ring and a single hexyloxy chain at the other end. They differ from each other in the halogen substitution pattern used at the single alkylated end, where fluorine at different positions was used. The fluorine atom was also replaced by chlorine or bromine atoms to investigate the effect of different types of halogen substituents on the phase behaviour. The molecular self-assembly of the materials was investigated using differential scanning calorimetry, polarized optical microscopy, X-ray diffraction and fluorescence techniques. Depending on the type and position of the halogen substituent, different types of mesophases were observed, including nematic, smectic, and chiral isotropic liquid phase ($\mathrm{Iso}_1^{[*]}$) and achiral double-gyroid bicontinuous cubic phases with a double helical network structure and $Ia\bar{3}d$ symmetry. In particular, the steric effect of halogen substituents adapts two different molecular packing for the cubic phase with local helicity and short-range order, respectively. All materials are fluorescent active, and their fluorescence behaviour could be altered by the type and position of the halogen substituent. Thus, this report provides new functional materials, which could be of interest for optoelectronic applications.

1. Introduction

Liquid crystalline (LC) materials with stimuli-responsive properties provide important access to responsive functional materials.[1] Therefore, π-conjugated LC materials[2–6] are known for their several applications as for example photodetectors,[7–9] photovoltaic cells,[10,11] light-emitting diodes,[12,13] and thin-film transistors.[14–16] The presence of a hetero atom such as sulphur, nitrogen or oxygen in the aromatic backbone induces polarizability in the whole system.[17] For this reason, different types of heterocyclics were used to design a wide variety of luminescent and photoconductive LCs such as oxadiazole and thiophene five-membered rings.[18–23] Thiophene-based π-conjugated materials can offer enhanced performance in organic electronic devices.[24–26] The thiophene ring introduces significant local dipole moment and thus stabilises the LC structure and also increases the dielectric anisotropy. It is known for its fluorescence properties[27,28] and has been applied for designing different classes of thermotropic LCs. Thus, it has been used for calamitic,[29–32] discotic,[27] and bent-core molecules[33–35] and polycatenars.[36] In recent years bithiophene-based polycatenars have attracted significant interest due to their ability to exhibit chiral LC phases in achiral materials.[37–42] These molecules were proved to form chiral bicontinuous cubic phases composed of triple networks with $I23$ symmetry ($\mathrm{Cub_{bi}}/I23^{[*]}$)[43] as well as the double-gyroid $\mathrm{Cub_{bi}}$ phase with the $Ia\bar{3}d$ space group ($\mathrm{Cub_{bi}}/Ia\bar{3}d$).[44] They are also able to display mirror-symmetry breaking in their isotropic liquid phases assigned as $\mathrm{Iso}_1^{[*]}$.

Generally, structural modification plays a very important role in molecular packing and self-organization in the LC phase. One way to modify the phase behaviour is lateral substitution at different positions and numbers.[45,46] This strategy modifies the overall dipole moment and the molecular shape, which in turn influences the phase behaviour. Recently, we have reported a luminescent and photoconductive bithiophene-based tricatenar (**AHH**, Table 1) and its related analogues.[47] We were successfully able to demonstrate a protype of optoelectronic devices for these materials.

---

[a] Institute of Chemistry, Martin Luther University Halle-Wittenberg, 06120 Halle, Germany. E-mail: mohamed.alaasar@chemie.uni-halle.de
[b] Department of Chemistry, Faculty of Science, Cairo University, 12613 Giza, Egypt. E-mail: malaasar@sci.cu.edu.eg
[c] Shaanxi International Research Center for Soft Matter, State Key Laboratory for Mechanical Behavior of Materials, Xi'an Jiaotong University, Xi'an 710049, P. R. China
[d] Guangdong Provincial Key Laboratory of Functional and Intelligent Hybrid Materials and Devices, Guangzhou 510641, China
[e] Organic Chemistry, University of Duisburg Essen, Universitätsstraße 7, Essen 45117, Germany. E-mail: michael.giese@uni-due.de

† Electronic supplementary information (ESI) available. See DOI: https://doi.org/10.1039/d4ma00771a

© 2024 The Author(s). Published by the Royal Society of Chemistry

Open Access Article. Published on 24 September 2024. Downloaded on 2/13/2026 4:09:46 PM. This article is licensed under a Creative Commons Attribution 3.0 Unported Licence.

Table 1 Phase transitions of compounds **AXY**[a]

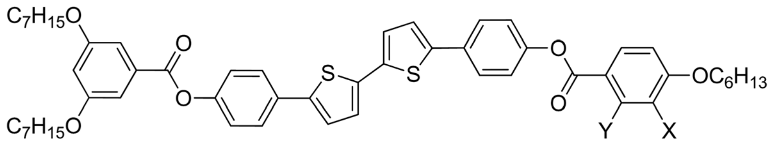

Cpd.	X	Y	Phase transitions T/°C [ΔH/kJ mol^{-1}]
AHH[47]	H	H	H: Cr 121 [30.7] SmC 197 [1.4] Iso$_1^{[*]}$ 200 [<0.1] Iso C: Iso 198 [<0.1] Iso$_1^{[*]}$ 193 [−1.8] SmC 89 [−25.0] Cr
AFH	F	H	H: Cr 117 [33.8] Cub$_{bi}$/$Ia\bar{3}d$ 200 [2.4] Iso C: Iso 191 [−2.1] Cub$_{bi}$/$Ia\bar{3}d$ 70 [−21.1] Cr
AHF	H	F	H: Cr 112 [35.4] SmC 171 [1.3] N 190 [0.4] Iso C: Iso 188 [−0.5] N 169 [−0.8] N$_x$ 166 [−0.3] SmC 33 [−7.8] Cr
AFF	F	F	H: Cr 118 [37.9] Cub$_{bi}$/$Ia\bar{3}d$ 195 [2.3] Iso C: Iso 188 [−0.7] Iso$_1^{[*]}$ 175 [−1.3] Cub$_{bi}$/$Ia\bar{3}d$
AHCl	H	Cl	H: Cr 113 [23.6] SmC 131 [0.2] N 136 [0.8] Iso C: Iso 132 [−0.9] N 131 [<0.1] SmC 46 [−15.8] Cr
AHBr	H	Br	H: Cr 126 [43.3] Cub$_{bi}$/$Ia\bar{3}d$ 134 [1.8] Iso C: Iso 124 [−1.1] SmC 117 [−0.3] Cub$_{bi}$/$Ia\bar{3}d$ 69 [−29.6] Cr

[a] Peak temperatures as determined by DSC upon 2nd heating (H:) and 2nd cooling (C:) at a rate of 10 K min^{-1}. Abbreviations: Cr = crystalline solid phase; Iso = isotropic liquid phase; Iso$_1^{[*]}$ = isotropic liquid phase with spontaneously broken symmetry; N = nematic phase; N$_x$ = unknown nematic phase; SmC = smectic C phase; Cub$_{bi}$/$Ia\bar{3}d$ = achiral bicontinuous cubic phase with the $Ia\bar{3}d$ space group.

Herein, we report a new type of such 5,5′-diphenyl-2,2′-bithiophene-based tricatenars having the same aromatic backbone with a 3,5-diheptyloxy substituted-benzene ring at one end and a single hexyloxy chain at the other end (**AXY**, Table 1). The materials differ from each other in the halogen substitution pattern used at the single alkylated end, where the fluorine atom was used at the *ortho*, *meta* or both positions with respect to the hexyloxy chain at the mono-terminated benzene ring (compounds **AFH**, **AHF**, and **AFF**, respectively). In the remaining materials, the F atom in **AHF** was replaced by chlorine (**AHCl**) or bromine (**AHBr**). Therefore, different halogen substitution patterns were used to successfully manipulate the phase behaviour of the parent molecule (**AHH**). Moreover, we investigate the fluorescence properties of the new materials in detail to demonstrate their potential applications.

2. Experimental details

2.1. Synthesis

The synthesis of the new materials was performed as shown in Scheme 1. The synthesis details and related analytical data are provided in the ESI.†

2.2. Characterization methods

Analytical quality chemicals were obtained from commercial sources and used as obtained. The solvents were dried using the standard methods when required. The purity and the chemical structures of all synthesised materials were confirmed by the spectral data. The structural characterization of the prepared materials is based on ^{1}H-NMR, ^{13}C-NMR and ^{19}F-NMR (Agilent Technologies 400 MHz VNMRS and 500 MHz DD2 spectrometers, in $CDCl_3$ solution) studies. ^{1}H-NMR and ^{13}C-NMR chemical shifts are reported in ppm referenced to tetramethylsilane. The residual proton signal of the deuterated solvent was used as the internal standard for ^{1}H NMR and ^{13}C-NMR spectra. ^{19}F NMR chemical shifts are reported in ppm referenced to trichlorofluoromethane as an external standard.

Polarized optical micrographs (POMs) were acquired under the crossed Nicol's condition. Differential scanning calorimetry (DSC) traces were measured with DSC-7 and DSC-8000 PerkinElmer setups, under an Ar flow, at a heating or cooling rate of 10 K min^{-1}. X-ray diffraction (XRD) patterns were recorded using Cu Kα radiation in the small-angle X-ray scattering (SAXS) and wide-angle X-ray scattering (WAXS) configurations.

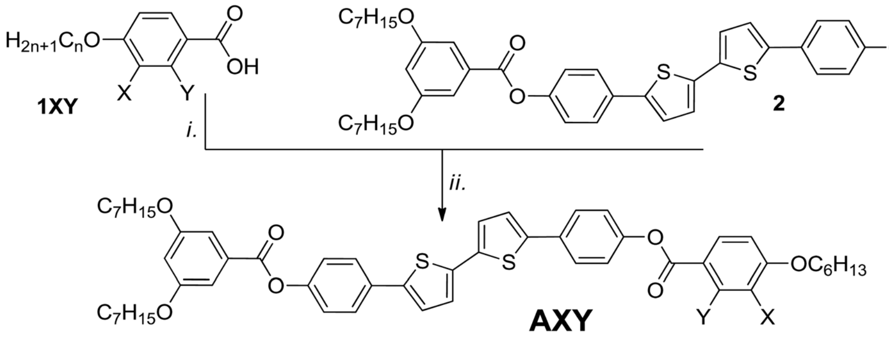

Scheme 1 Synthesis of the reported materials **AXY**. *Reagents and conditions*: (i) $SOCl_2$ and (ii) triethylamine, pyridine, DCM, reflux.

© 2024 The Author(s). Published by the Royal Society of Chemistry

Open Access Article. Published on 24 September 2024. Downloaded on 2/13/2026 4:09:46 PM.
This article is licensed under a Creative Commons Attribution 3.0 Unported Licence.

Fluorescence spectra were acquired with an RF-6000 from Shimadzu Corporation.

3. Results and discussion

The mesophase types and phase transition temperatures with associated enthalpy values recorded on heating and cooling of the reported materials **AXY** are gathered in Table 1. Combined results from DSC and POM are represented graphically in Fig. 1. The DSC thermograms of all materials are given in the ESI.†

3.1. Thermal and liquid crystalline behavior

As can be seen from Table 1 and Fig. 1, all materials are liquid crystalline exhibiting different types of LC phases depending on the type of the halogen substituent. In all cases, the melting and crystallization temperatures of the new materials are lower compared to those of the parent molecule **AHH**, resulting in wider LC ranges. Compound **AFH** with one F atom at the *ortho* position with respect to the terminal hexyloxy chain exhibits one LC over a wide temperature range. This phase is characterized under POM by its high viscosity and homeotropic appearance under crossed polarizers (Fig. 2(e)). Under slightly uncrossed polarizers either in clockwise or anticlockwise directions, no chiral domains could be observed, meaning the presence of an achiral three-dimensional LC phase. These are typical observations for the double-gyroid bicontinuous cubic phase, which was further confirmed *via* XRD investigations (Section 3.2).

Changing the position of the F atom in **AFH** from *ortho* to *meta* in compound **AHF** results in the removal of the cubic phase and the appearance of three different LC phases. On cooling from the isotropic state, a marble texture is observed (Fig. 2(c)), which is highly fluid and flashes on applying shearing stress indicating the presence of a nematic phase. On cooling this N phase, the green colour changes to yellowish-red colour (Fig. 2(d)) indicating the transition to another LC phase associated with a small transition peak in the DSC curve (Fig. S15, ESI†). This metastable phase with a narrow temperature range of ~3 K could not be investigated in more detail *via* XRD (see the light green region in Fig. 1). Based on this information it is assigned as the N_x phase. On further cooling the viscosity is increased and the marble texture is replaced by a schlieren one, which is characteristic of a smectic phase (Fig. 2(f)). This phase was proved further by XRD (Section 3.2) and remains over ~133 K and crystallizes close to room temperature at ~33 °C.

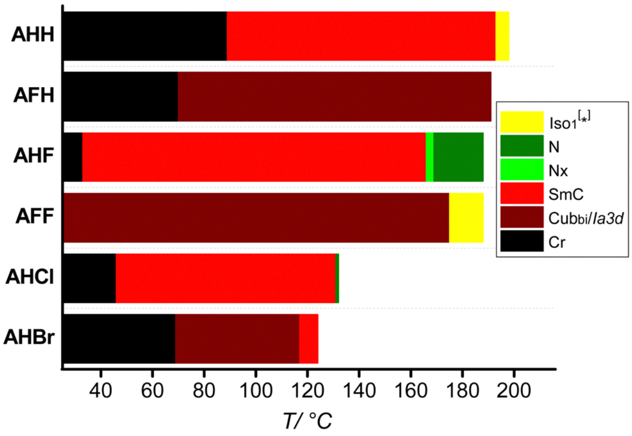

Fig. 1 Phase transitions of **AXY** compounds as observed on 2nd cooling at a rate of 10 K min^{-1}.

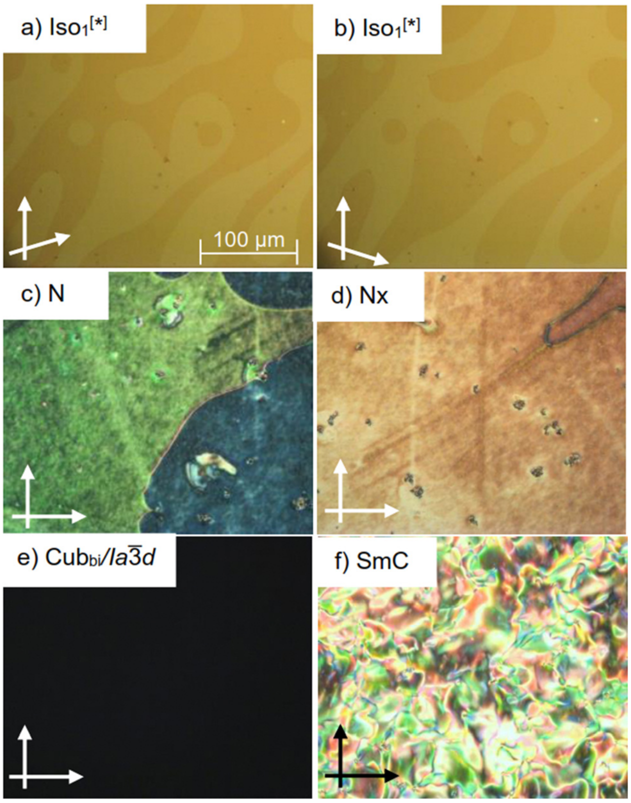

Fig. 2 Optical micrographs on cooling for: (a) and (b) the chiral $Iso_1^{[*]}$ phase at 185 °C of compound **AFF** under slightly uncrossed polarizers either in a clockwise or in an anticlockwise direction (see white arrows); (c) the N phase of compound **AHF** at 183 °C; (d) the N_x phase of compound **AHF** at 168 °C; (e) the double-gyroid achiral $Cub_{bi}/Ia\bar{3}d$ phase of compound **AFH** at 90 °C and (f) the schlieren texture in the SmC phase of compound **AHF** at 140 °C.

Introducing two F atoms at both *ortho* and *meta* positions in case of **AFF** results in stabilization of the cubic phase, which once formed on heating does not recrystallize on cooling down to room temperature. The crystallization of this phase is only observed on reheating the sample (Fig. S16, ESI†). For this compound mirror-symmetry breaking is observed in the isotropic liquid on cooling from the isotropic state (Fig. 2(a) and (b)). On cooling under slightly uncrossed polarizers dark and bright domains could be observed in the highly fluid liquid phase. Inverting the direction of the rotation of one of the analysers results in inversion of the sign of the dark and bright domains indicating the chirality of this liquid phase. These are the typical observations for the $Iso_1^{[*]}$ reported for the non-substituted compound **AHH** and its related homologues.[42] Thus this phase is also assigned as the $Iso_1^{[*]}$ phase. Such chirality is introduced by the twisting aromatic core and

© 2024 The Author(s). Published by the Royal Society of Chemistry

Open Access Article. Published on 24 September 2024. Downloaded on 2/13/2026 4:09:46 PM. This article is licensed under a Creative Commons Attribution 3.0 Unported Licence.

asymmetrical aliphatic chains, which supports the formation of molecular helices. Such helices require a suitable ratio between the volume of aromatic core and aliphatic chains, commonly found for bicontinuous cubic network phases.[48,49] In our case, two $\mathrm{Iso}_1^{[*]}$ phases are found for **AHH** and **AFF**. For **AHH**, aliphatic chain volume expansion at high temperatures leads to the molecular helices as those shown in **AFH** (Fig. 3(c)). Molecular helices for **AFF** are simply the result of a disorder of the low temperature $\mathrm{Cub_{bi}}/Ia\bar{3}d$ phase.

To further investigate the effect of other halogen atoms, we synthesized additional two compounds related to **AHF**. In these two materials, the fluorine atom was replaced by a chlorine or bromine atom. In the chlorinated material (**AHCl**) similar phase sequence to **AHF** is observed, where only N and smectic phases are formed. However, the LC phase range is greatly reduced owing to the larger size of the Cl atom compared to the F one. This results in a more steric effect in the case of **AHCl**, which in turn leads to less dense packing of the aromatic cores. This was also the case for the brominated material (**AHBr**), which exhibits also short range of LC phase compared to **AHF** or **AHCl** because of the larger size of the bromine atom (more than Cl or F). However, the nematic phase observed for **AHF** or **AHCl** is replaced by the cubic one.

Therefore, from these observations, core fluorination is the most effective tool to modify and stabilize the LC phases in such types of polycatenars compared to other halogen substituents.

3.2. XRD investigations

Peripheral fluorinated compounds **AFH** self-assembled into the achiral $\mathrm{Cub_{bi}}/Ia\bar{3}d$ phase. The fluorination induced a steric effect which is critical to the formation of the $\mathrm{Cub_{bi}}/Ia\bar{3}d$ phase. The SAXS diffractogram of **AFH** exhibits a series of scattering peaks of typical ratio with the $Ia\bar{3}d$ space group (Fig. 3(a)). The reconstructed electron density (ED) map in Fig. 3(b) clearly suggests the morphology of a double gyroid (DG) network separated by a G minimal surface. Polycatenars are stacked into rafts with 3–4 molecules and then assembled into a molecular helix along the high ED networks in purple.

Due to the halogens with high ED, the networks in the ED map are not fully isolated as normal DG networks formed by polycatenars. A simplified model is presented in Fig. 3(c), where networks with opposite chirality are shown in red and blue and the G minimal surface is shown in yellow. With aromatic cores aligned perpendicular to networks, aliphatic tails reach the minimal surface to minimize the overall free energy. Molecular helices of opposite helicity progress along two networks with opposite handedness. Pinned by the three-way junctions, the short-range molecular helix can nicely transport the helicity along the infinite network. With a lattice parameter of 9.75 nm, the segment length between neighbouring three-way junctions is 3.45 nm (Table S7, ESI†). Since the dihedral angle of neighbouring three-way junctions is fixed at 70.5°, the twisting angle and number of molecules per raft become 9.2° and 3.4 on average. Compared with the non-fluorinated compound **AHH**, peripheral fluorination pushes the phase to 3D bicontinuous network phases. Such transition is induced by the steric effect of peripheral fluorination which generates a molecular helix to avoid the clashing of fluorine atoms.

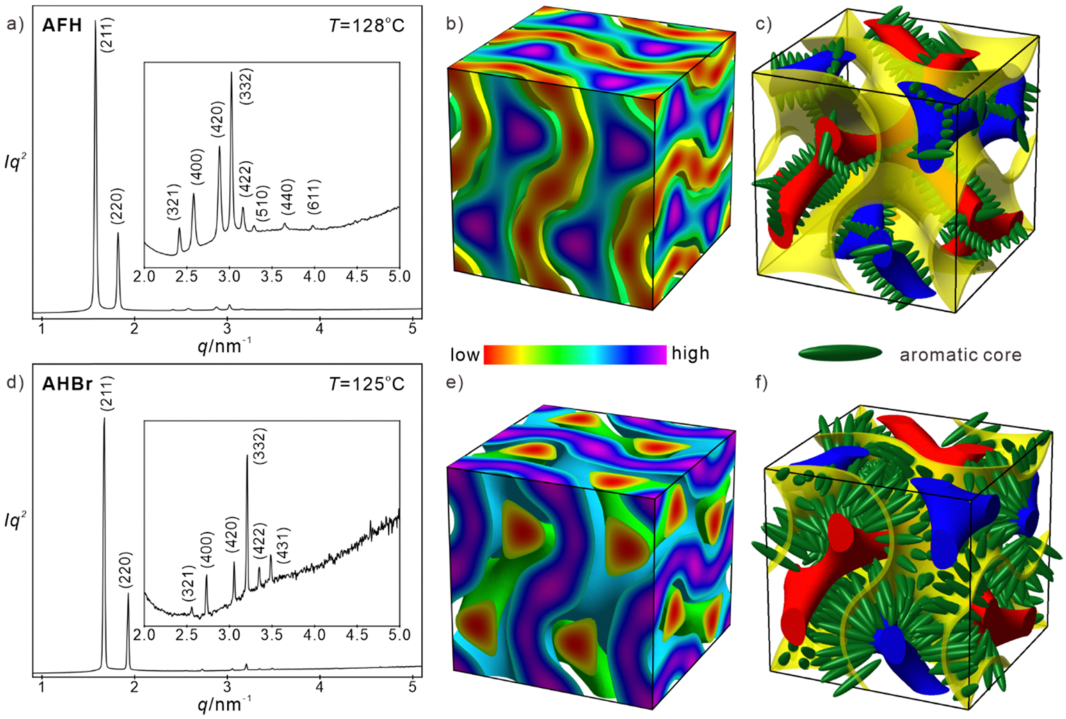

Fig. 3 SAXS diffractograms of the $\mathrm{Cub_{bi}}/Ia\bar{3}d$ phase for (a) **AFH** at 128 °C and (d) **AHBr** at 125 °C; (b) and (e) the reconstructed ED maps for two compounds, high ED is in purple and low ED is in red; and (c) and (f) the schematic model of molecular packing for two compounds.

© 2024 The Author(s). Published by the Royal Society of Chemistry

Open Access Article. Published on 24 September 2024. Downloaded on 2/13/2026 4:09:46 PM.
This article is licensed under a Creative Commons Attribution 3.0 Unported Licence.

Apart from **AFH**, **AFF** with inside directed halogens also exhibits the same Cub$_{bi}$/$Ia\bar{3}d$ phase, whose lattice parameter is 9.64 nm at 128 °C. Similarly, the average twisting angle and molecules per raft can be derived as 9.3° and 3.2. The slight expansion of the twisting angle and decrease of molecules per raft suggest less ordered packing in the molecular raft. It's well known that inside directed halogens destabilize the lamellar phase and favour the less ordered nematic phase due to the bulky halogen size. Such an effect also influences the Cub$_{bi}$/$Ia\bar{3}d$ phase. The $T_{\text{Cub–Iso}}$ of **AFF** (195 °C) is lower than that of **AFH** (200 °C). While the Cub$_{bi}$/$Ia\bar{3}d$ phase is not rare for polycatenars, molecules normally form helices progressing along the network in the *meso*-structure. **AHBr** is the first case with molecules arranged along the minimal surface instead of networks, as a frustrated state of the lamellar phase.

However, if considering inside directed halogens solely, **AHF** exhibits totally different phase behaviour. Only one single scattering peak can be found in SAXS at low temperatures, suggesting a lamellar phase with the lattice parameter as large as 3.84 nm. Considering the molecular size of **AHF**, the reconstructed ED map suggests a tilting aromatic core (Fig. 4(a)), *i.e.* a SmC phase. The SmC phase is also supported by the increasing lattice parameter upon heating, which originates from the decreasing tilt angle of molecules (Fig. 4(b)).

Upon further heating, a phase transition to nematic occurs, supported by the significant decrease in coherence (Fig. 4(b)). The nematic phase is introduced by inside directed fluorination and **AHCl** (131 °C) exhibits an even lower $T_{\text{SmC–N}}$ and a narrower temperature range of the SmC phase compared with **AHF** (171 °C). Moreover, the *d*-spacing of the SmC phase decreases with the halogen size, 3.68 nm for **AHCl** and 3.51 nm for **AHBr**, originating from the bulky size and stronger in-layer deformation.

Surprisingly, **AHBr** with even larger inside directed halogen forms the Cub$_{bi}$/$Ia\bar{3}d$ phase (Fig. 3(d)) again instead of the nematic phase. The lattice parameter of the Cub$_{bi}$/$Ia\bar{3}d$ phase is 9.19 nm at 125 °C. Judged from the radial volume distribution curve dV/dr, the furthest point is ~3.5 nm away from the double gyroid network (Fig. S23, ESI†), which is close to the length of the aromatic core (3.45 nm, measured by Materials Studio). Thus, common molecular packing with twisting rafts requires strong intercalation and deformation of the aliphatic tail or molecular tilting as the SmC phase. Both are unlikely to generate a stable cubic phase with the molecular helix due to mismatch at junctions. Instead, if the aromatic cores are packed loosely along the minimal surface (Fig. 3(e) and (f)), the distance between networks is 3.98 nm. Measured from the ED map, the thickness of the high ED region between networks is ~1.92 nm, *i.e.* aromatic cores are tilted in the high ED region. The area of the G minimal surface can be calculated as ~207 nm^2[50] and the number of molecules per cell is ~484. Thus, each molecule occupies ~0.4 nm^2. The area of the aromatic core intersection is roughly estimated to be 0.2 nm^2 (V_{mol}/3.45 = 0.17 nm^2). Considering the molecular tilting, each molecule occupies ~0.36 nm^2, supporting the molecular packing model along the minimal surface (Fig. 3(f)).

3.3. Photophysical investigations

To investigate the fluorescence behaviour of the new series of bithiophene-based polycatenars we initially performed fluorescence spectroscopy in the solid state at room temperature. The whole series of compounds showed blue to green fluorescence at room temperature in the region from 480 to 520 nm (Fig. 5).

Furthermore, **AHH**, **AHF**, **AFH**, **AFF**, and **AHCl** show two clear emission signals, the first one between 480 and 490 nm and the second one between 505 and 520 nm (Fig. 6(a) and Fig. S24, S25, ESI†) with a shoulder at ~550 nm. For **AHBr** a distinct signal at 550 nm (Fig. 6(b)) was observed. For **AHF** and **AFF**, we observed the global maxima at around 480 nm while for **AHH**, **AFH**, **AHCl**, and **AHBr**, the global maxima were observed between 505 and 520 nm. This indicates that different fluorination patterns and the nature of the halogen substituent have an impact on the emissive behaviour of the polycatenars.

Comparing the impact of fluorination on the relative emission intensity, we observe an increased intensity for the fluorinated materials in comparison with **AHH** (Fig. S26, ESI†). While *ortho*-fluorination (**AFH**) only leads to a small increase, the *meta*-fluorinated material **AHF** shows a relative emission intensity that is higher than that of the unsubstituted **AHH**. Further fluorination enhances this effect. The di-fluorinated **AFF** exhibits

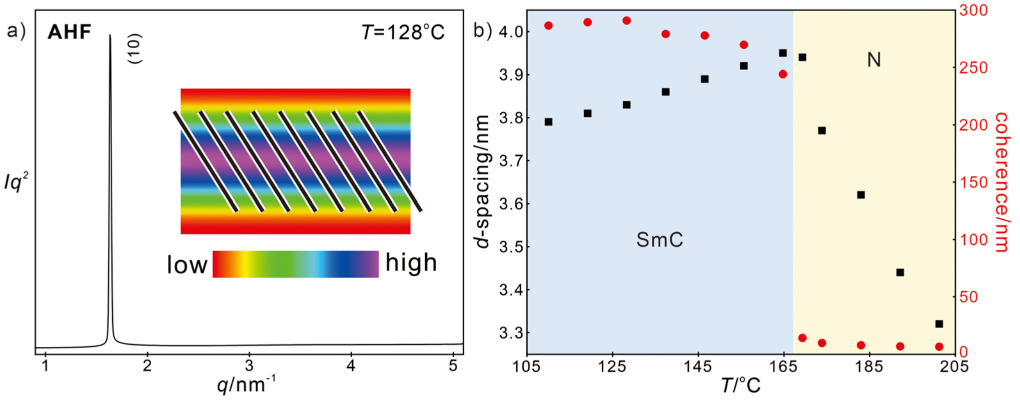

Fig. 4 (a) SAXS diffractograms of the SmC phase for **AHF** at 128 °C and (b) temperature dependence of *d*-spacing and coherence of **AHF** upon heating.

Open Access Article. Published on 24 September 2024. Downloaded on 2/13/2026 4:09:46 PM.
This article is licensed under a Creative Commons Attribution 3.0 Unported Licence.

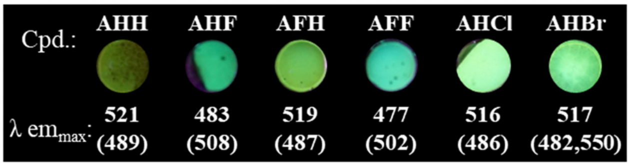

Fig. 5 Global and local emission maxima for all studied polycatenars, with photographs under UV-light (395 nm) at room temperature.

a relative emission intensity higher than that of the *meta*-fluorinated **AHF** and the unsubstituted **AHH** respectively. Regarding the wavelength of the global emission maxima, *meta-* (**AHF**) and di-fluorination (**AFF**) lead to a hypsochromic shift from 521 nm to around 480 nm. In contrast, *ortho*-fluorination (**AFH**) has no significant impact on the location of emission maxima.

Comparing the different halogen substituted compounds with each other reveals a significant impact on the intensities of the emission maxima of investigated materials. In general, *meta*-halogenation leads to an increase in the relative intensity of the emission maxima compared to **AHH**. In the series **AHF**, **AHCl** and **AHBr**, the **AHCl** derivative shows the lowest emission intensity while **AHBr** exhibits the highest value. For the location of the global emission maxima, we observe no significant impact on *meta*-chlorination or -bromination. Only the *meta*-fluorination led to the already described hypsochromic shift.

Since fluorescence behaviour strongly depends on the molecular packing of the materials, variable temperature fluorescence measurements were performed to investigate the emission properties in the different phases – solid phase, mesophase and isotropic phase. Thin films of the materials between two glass slides were prepared by heating the crystalline materials to the isotropic state on a glass substrate. After cooling, the samples were kept for 24 h at room temperature. Subsequently, the samples were thermally treated starting at 30 °C until they reached their respective clearing points and then cooled back to 30 °C. Fluorescence spectra were collected at every $\Delta T = 10$ °C. Starting with **AHH** as the unsubstituted reference (Fig. 7), we observe a decreasing intensity of both emission signals with rising temperature until 120 °C, which is characteristic of AIE luminophores.[51,52] At 130 °C, the material exhibits the SmC-phase and the two emission signals (489/522 nm) merge to one signal with increased intensity at 509 nm (Fig. 7(b)). Upon further heating to 170 °C, **AHH** yields an increase in the emission maxima, followed by the characteristic decrease in emission intensity for AIE luminophores until 200 °C. Upon cooling (Fig. 7(c)), the intensity of the emission maxima decreases in the temperature range of 200 °C to 180 °C. After passing the chiral isotropic phase at 193 °C and in the SmC phase, the intensity of the emission maxima starts to rise again until 100 °C. Below 90 °C, the material returns to its crystalline phase and two emission signals in the region from 480 to 490 nm and 510 to 520 nm were observed. This change from the emission maxima is linked with a rapid drop in the relative emission intensity. Subsequently, the intensity of the signals increases slightly with decreasing temperature until reaching 30 °C. The temperature-dependent measurements of the emission show that **AHH** does not behave like a typical AIE emitter. As indicated by the self-assembly structure, halogen substitution exhibits a clear steric effect, which induces the phase transition from the smectic phase to the cubic phase. The steric effect leads to either local twist or short-range disorder, which decreases the intermolecular interaction and results in the special AIE property.

The series of *ortho-* (**AFH**), *meta-* (**AHF**) and di-fluorinated (**AFF**) materials showed a similar emission behaviour at varying temperatures to **AHH** (Fig. 8 and Fig. S27, S28, ESI†). All fluorinated materials showed a likewise merging/shift of the emission maximum after the transition into the mesophase upon heating. **AFH** shows like **AHH** a blue shift of the global emission maximum from 519 (487) nm to 512 nm and a sharp emission signal at 120 °C which correlates with the transition into the LC phase. In contrast, **AHF** and **AFF** exhibit a redshift of the global emission maxima upon entering the mesophase at 112 °C (**AHF**) and 118 °C (**AFF**) respectively.

In addition, the emission maximum of **AFF** shifts even further after entering the liquid crystalline state from 508 nm at 140 °C to 516 nm at 160 °C. *ortho*-Fluorination (**AFH**) leads to a smaller shift of the global emission maximum in comparison with the unsubstituted **AHH** under thermal treatment. The *meta-* (**AHF**) and di-fluorination (**AFF**) lead to a larger shift of

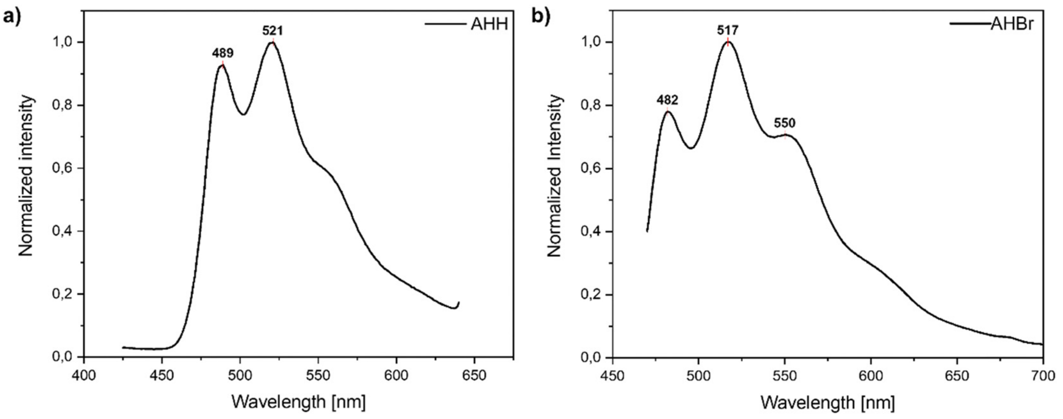

Fig. 6 Normalized emission spectra of solid-state emission of **AHH** (a, excitation wavelength 332 nm) and **AHBr** (b, excitation wavelength 450 nm) as representative examples of the fluorescence behaviour of the different polycatenars at room temperature.

© 2024 The Author(s). Published by the Royal Society of Chemistry

Open Access Article. Published on 24 September 2024. Downloaded on 2/13/2026 4:09:46 PM. This article is licensed under a Creative Commons Attribution 3.0 Unported Licence.

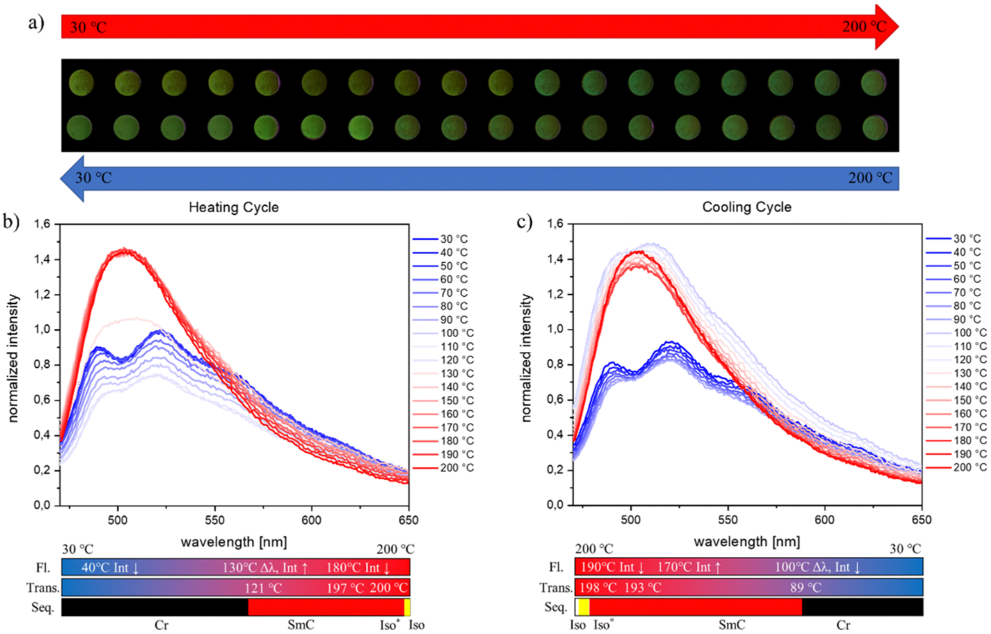

Fig. 7 (a) Photographs of **AHH** during heating and cooling under UV-light (395 nm). Pictures were taken every 10 °C for the heating and cooling cycles respectively. (b) Normalized emission spectra of **AHH** (excitation wavelength 450 nm) during the heating cycle. Starting with 30 °C, data were collected every 10 °C until reaching 200 °C. (c) Normalized emission spectra of **AHH** (excitation wavelength 450 nm) during the cooling cycle. Starting with 200 °C, data were collected every 10 °C until reaching 30 °C.

the emission wavelength which is also visible to the naked eye. In the cases of **AFH** and **AHF,** the transition into the mesophase is accompanied by an increase in emission intensity which is more prominent when compared to **AHH** (compare Fig. 7 and Fig. S27, S28, ESI†). **AFF** does not show such an increase (Fig. 8). For **AFH** exhibiting the SmC phase, the intensity is more than doubled while for **AHF** displaying the cubic phase we could observe an increase of around 40%. This means that derivatives displaying cubic phases are less active compared to those exhibiting SmC phases. Therefore, there is a stronger

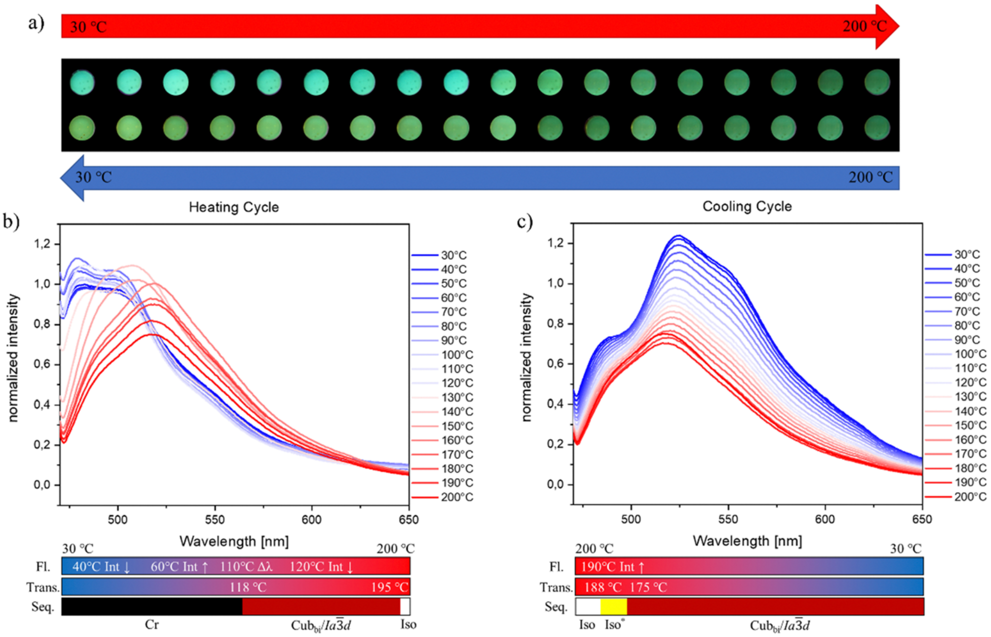

Fig. 8 (a) Photographs of **AFF** during heating and cooling under UV-light (395 nm). Pictures were taken every 10 °C for the heating and cooling cycles respectively. (b) Normalized emission spectra of **AFF** (excitation wavelength 450 nm) during the heating cycle. Starting with 30 °C, data were collected every 10 °C until reaching 200 °C. (c) Normalized emission spectra of **AFF** (excitation wavelength 450 nm) during the cooling cycle. Starting with 200 °C, data were collected every 10 °C until reaching 30 °C.

Open Access Article. Published on 24 September 2024. Downloaded on 2/13/2026 4:09:46 PM.
This article is licensed under a Creative Commons Attribution 3.0 Unported Licence.

effect of *meta*-fluorination and mono-fluorination in general at the respective positions as it could alter the type of LC phase, which in turn could change the emission intensity. Upon further heating, all materials showed the same characteristic intensity decrease of the emission maxima. During the cooling process, all materials displayed an increase in the intensity of the emission maxima. In the same fashion as **AHH**, the mono-fluorinated materials **AFH** and **AHF** show a broadening of the emission spectra upon further cooling before entering the crystalline phase. For **AFH,** this change was observed between 200 °C and 90 °C (Fig. S27, ESI†). With the start of the crystallization process, the intensity decreases and the signal splits into two local maxima at 80 °C. At 30 °C the sample returned to its initial state. In the case of **AHF**, the increase and broadening of the signals are observed between 190 °C and 50 °C and it returns to its initial spectra at 40 °C. In contrast to the described materials, **AFF** displays a continuous increase in the intensity of the emission maximum. In addition, the emission enhancement and the red shift of the emission wavelength are preserved upon cooling to 30 °C (Fig. 8), which is attributed to the stabilization of the cubic phase down to ambient temperature without crystallization as confirmed by DSC investigations (Fig. S16, ESI†). This was not the case for any other investigated material. After maintaining **AFF** at room temperature for a long time (>48 hours), the sample crystallized and returned to its initial emission behaviour, which is again in agreement with DSC measurements.

meta-Substitution with chlorine (**AHCl**) or bromine (**AHBr**) also led to emissive materials whose emission is strongly dependent on the thermal treatment (Fig. 9 and Fig. S29, ESI†). For both materials, multiple emission signals and a decrease in the signal intensities before reaching the transition temperature to the mesophase were observed. For **AHCl** a small blue shift of the emission wavelength and merging of the two emission signals at 110 °C were observed. This merge of the multiple emission maxima in combination with a shift of the global emission wavelength matches the earlier described behaviour of the *meta*-fluorinated (**AHF**) and the unsubstituted (**AHH**) samples. In contrast, the *meta*-bromination (**AHBr**) leads to a material that does not show a shift in the global emission maxima upon thermal treatment. Nevertheless at 110 °C to 120 °C after the transition into the LC phase, the emission signals of **AHBr** merge into one signal, which is consistent with all investigated materials. While **AHH** and **AHF** showed an intensity increase of the emission maxima, **AHCl** showed no change in the emission intensity upon entering the LC phase. For the *meta*-brominated material **AHBr**, this effect is most concise (Fig. 9). At 120 °C where the transition to the cubic phase is expected, the intensity of the emission maximum already rises about 50% of the initial one at 30 °C. Upon further heating, this increase becomes even stronger, where at 130 °C an emission intensity which is three times higher than the initial one at 30 °C before the thermal treatment is observed. Upon cooling we see at first the characteristic AIE behaviour with an increasing emission intensity. At 130 °C an unexpected drop of the emission intensity is observed. Immediately after that the characteristic trend is restored. This is followed by the signal splitting into three local emission maxima and a decrease in emission intensity at the crystallization point of 70 °C. As for all *meta*-substituted materials

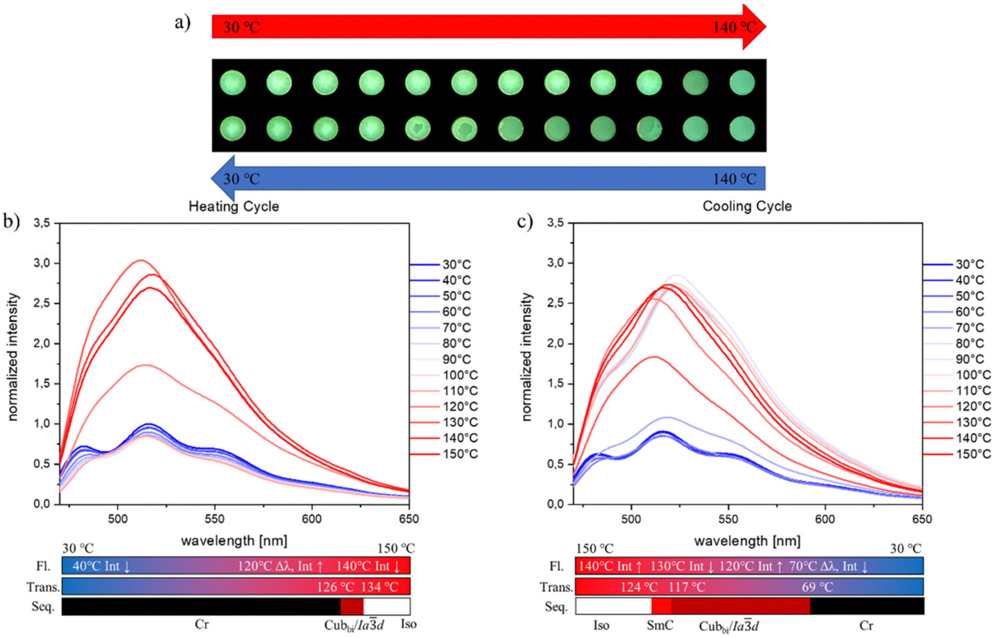

Fig. 9 (a) Photographs of **AHBr** during heating and cooling under UV-light (395 nm). Pictures were taken every 10 °C for the heating and cooling cycles respectively. (b) Normalized emission spectra of **AHBr** (excitation wavelength 450 nm) during the heating cycle. Starting with 30 °C, data were collected every 10 °C until reaching 150 °C. (c) Normalized emission spectra of **AHBr** (excitation wavelength 450 nm) during the cooling cycle. Starting with 150 °C, data were collected every 10 °C until reaching 30 °C.

© 2024 The Author(s). Published by the Royal Society of Chemistry

Open Access Article. Published on 24 September 2024. Downloaded on 2/13/2026 4:09:46 PM.
This article is licensed under a Creative Commons Attribution 3.0 Unported Licence.

the initial emission properties are restored after a completed cooling cycle to 30 °C.

4. Summary and conclusion

In summary, new functional π-conjugated 5,5′-diphenyl-2,2′-bithiophene-based tricatenars have been synthesized and characterized. The materials differ from each other in the halogen substituent used at one end of the molecular structure. Different types of halogen atoms were used including fluorine, chlorine or bromine groups. It was shown that the molecular packing of these polycatenars can be modulated by the type of the halogen atom (F, Cl or Br) or its number (two F instead of one). Indeed, rich polymorphism was observed in these LC materials, including nematic, smectic, and achiral double-gyroid bicontinuous cubic phases with a double helical network structure and $Ia\bar{3}d$ symmetry or chiral isotropic liquid phase ($\text{Iso}_1^{[*]}$). All phases were characterized by polarized optical microscopy, differential scanning calorimetry and XRD techniques. Moreover, the materials were investigated in detail for their fluorescence properties at room temperature and at different temperatures in the LC phases. Remarkably, all reported compounds are fluorescent active, and their spectra depend strongly on the type of the LC phase which could be controlled by the type and position of the halogen substituent used. These fluorescent materials might be of interest for future applications in sensors and optical storage devices.

Data availability

The data supporting this article have been included as part of the ESI.†

Conflicts of interest

There are no conflicts to declare.

Acknowledgements

M. Alaasar acknowledges the German Research Foundation (DFG) for the financial support (AL2378/1-2, 424355983). M. G. acknowledges the DFG for generous financial support *via* the Heisenberg-Programme (GI882/5-1, 443479537). Y. Cao acknowledges the National Natural Science Foundation of China (No. 12204369), the Science and Technology Agency of Shaanxi Province (2023-YBGY-459) and the Guangdong Provincial Key Laboratory of Functional and Intelligent Hybrid Materials and Devices (2023-GDKLFIHMD-01). The authors thank beamlines BL16B1 at the Shanghai Synchrotron Radiation Facility (SSRF) for providing the beam time.

References

1 M. Alaasar, A. F. Darweesh, Y. Cao, K. Iakoubovskii and M. Yoshio, *J. Mater. Chem. C*, 2024, **12**, 1523.
2 W. Pisula, M. Zorn, J. Y. Chang, K. Müllen and R. Zentel, *Macromol. Rapid Commun.*, 2009, **30**, 1179.
3 T. Kato, M. Yoshio, T. Ichikawa, B. Soberats, H. Ohno and M. Funahashi, *Nat. Rev. Mater.*, 2017, **2**, 17001.
4 H. K. Bisoyi and Q. Li, *Prog. Mater. Sci.*, 2019, **104**, 1.
5 A. S. Achalkumar, P. K. Behera, F.-R. Chen and J.-H. Jou, *J. Mater. Chem. C*, 2024, **12**, 8282–8286.
6 V. K. Vishwakarma, M. Roy, R. Singh, D. S. S. Rao, R. Paily and A. A. Sudhakar, *ACS Appl. Electron. Mater.*, 2023, **5**, 2351.
7 M. Hecht, T. Schlossarek, M. Stolte, M. Lehmann and F. Würthner, *Angew. Chem., Int. Ed.*, 2019, **58**, 12979.
8 A. Calò, P. Stoliar, M. Cavallini, Y. H. Geets and F. Biscarini, *Org. Electron.*, 2011, **12**, 851.
9 M. Dechant, M. Lehmann, G. Uzurano, A. Fujii and M. Ozaki, *J. Mater. Chem. C*, 2021, **9**, 5689.
10 M. Kumar and S. Kumar, *Polym. J.*, 2017, **49**, 85.
11 M. Funahashi, *Mater. Chem. Front.*, 2021, **5**, 8265.
12 T. Yasuda, H. Ooi, J. Morita, Y. Akama, K. Minoura, M. Funahashi, T. Shimomura and T. Kato, *Adv. Funct. Mater.*, 2009, **19**, 411.
13 C. Keum, D. Becker, E. Archer, H. Bock, H. Kitzerow, M. Gather and C. Murawski, *Adv. Opt. Mater.*, 2020, **8**, 2000414.
14 H. Iino, T. Usui and J. Hanna, *Nat. Commun.*, 2015, **6**, 6828.
15 D. H. Kim, B.-L. Lee, H. Moon, H. M. Kang, E. J. Jeong, J.-I. Park, K.-M. Han, S. Lee, B. W. Yoo, B. W. Koo, J. Y. Kim, W. H. Lee, K. Cho, H. A. Becerril and Z. Bao, *J. Am. Chem. Soc.*, 2009, **131**, 6124.
16 O. Kwon, X. Cai, W. Qu, F. Liu, J. Szydlowska, E. Gorecka, M. J. Han, D. K. Yoon, S. Poppe and C. Tschierske, *Adv. Funct. Mater.*, 2021, **31**, 2102271.
17 B. Roy, N. De and K. C. Majumdar, *Chem. – Eur. J.*, 2012, **18**, 14560.
18 T. Ghosh and M. Lehmann, *J. Mater. Chem. C*, 2017, **5**, 12308.
19 A. Seed, *Chem. Soc. Rev.*, 2007, **36**, 2046.
20 R. De, J. De, S. P. Gupta, I. Bala, Ankita, Tarun, U. K. Pandey and S. K. Pal, *J. Mater. Chem. C*, 2023, **11**, 980.
21 N. Tober, T. Rieth, M. Lehmann and H. Detert, *Chem. – Eur. J.*, 2019, **25**, 15295.
22 B. Pradhan, R. K. Gupta, S. K. Pathak, J. De, S. K. Pal and A. S. Achalkumar, *New J. Chem.*, 2018, **42**, 3781.
23 K. Iakoubovskii and M. Yoshio, *Chem. Commun.*, 2023, **59**, 7443.
24 H. Dong, C. Wang and W. Hu, *Chem. Commun.*, 2010, **46**, 5211.
25 J. E. Anthony, *Chem. Rev.*, 2006, **106**, 5028.
26 W. Jiang, Y. Li and Z. Wang, *Chem. Soc. Rev.*, 2013, **42**, 6113.
27 Y. Li, A. Concellón, C.-J. Lin, N. A. Romero, S. Lin and T. M. Swager, *Chem. Sci.*, 2020, **11**, 4695.
28 X. Zhu, C. Hessin, A. Salamé, L. Sosa-Vargas, D. Kreher, C. Adachi, A. Proust, P. Mialane, J. Marrot, A. Bouchet, M. Sliwa, S. Méry, B. Heinrich and F. Mathevet, *Angew. Chem., Int. Ed.*, 2021, **60**, 8419.
29 M. P. Aldred, R. Hudson, S. P. Kitney, P. Vlachos, A. Liedtke, K. L. Woon, M. O'Neill and S. M. Kelly, *Liq. Cryst.*, 2008, **35**, 413.

© 2024 The Author(s). Published by the Royal Society of Chemistry

Open Access Article. Published on 24 September 2024. Downloaded on 2/13/2026 4:09:46 PM.
This article is licensed under a Creative Commons Attribution 3.0 Unported Licence.

30 C. Da Cruz, J. C. Rouillon, J. P. Marcerou and H. T. Nguyen, *Liq. Cryst.*, 2003, **30**, 1175.

31 K. C. Majumdar, T. Ghosh, S. Chakravorty, N. Pal, D. S. S. Rao and S. K. Prasad, *Liq. Cryst.*, 2010, **37**, 1539.

32 Z. Puterova, J. Romiszewski, J. Mieczkowski and E. Gorecka, *Tetrahedron*, 2012, **68**, 8172–8180.

33 K. Bajzíková, J. Veselý, V. Kozmík, J. Svoboda, V. Novotná and D. Pociecha, *J. Mol. Liq.*, 2018, **267**, 496.

34 A. J. Paraskos and T. M. Swager, *Chem. Mater.*, 2002, **14**, 4543.

35 K. Geese, M. Prehm and C. Tschierske, *J. Mater. Chem.*, 2010, **20**, 9658.

36 J. Matraszek, D. Pociecha, N. Vaupotič, M. Salamonczyk, M. Vogrine and E. Gorecka, *Soft Matter*, 2020, **16**, 3882.

37 C. Dressel, F. Liu, M. Prehm, X. B. Zeng, G. Ungar and C. Tschierske, *Angew. Chem., Int. Ed.*, 2014, **53**, 13115.

38 C. Dressel, T. Reppe, S. Poppe, M. Prehm, H. Lu, X. Zeng, G. Ungar and C. Tschierske, *Adv. Funct. Mater.*, 2020, 2004353.

39 T. Reppe, S. Poppe, X. Cai, Y. Cao, F. Liu and C. Tschierske, *Chem. Sci.*, 2020, **11**, 5902.

40 T. Reppe, C. Dressel, S. Poppe, A. Eremin and C. Tschierske, *Adv. Opt. Mater.*, 2021, **9**, 2001572.

41 M. Alaasar, A. F. Darweesh, X. Cai, Y. Cao, F. Liu and C. Tschierske, *Chem. – Eur. J.*, 2021, **27**, 14921.

42 A. Murad, M. Alaasar, A. F. Darweesh and A. Eremin, *Mater. Adv.*, 2024, **5**, 6205.

43 X. Zeng and G. Ungar, *J. Mater. Chem. C*, 2020, **8**, 5389.

44 Y. Cao, M. Alaasar, A. Nallapaneni, M. Salamończyk, P. Marinko, E. Gorecka, C. Tschierske, F. Liu, N. Vaupotič and C. Zhu, *Phys. Rev. Lett.*, 2020, **125**, 027801.

45 M. Alaasar, M. Prehm, Y. Cao, F. Liu and C. Tschierske, *Angew. Chem., Int. Ed.*, 2016, **128**, 320.

46 M. Alaasar, J. C. Schmidt, X. Cai, F. Liu and C. Tschierske, *J. Mol. Liq.*, 2021, **332**, 115870.

47 M. Alaasar, A. F. Darweesh, C. Anders, K. Iakoubovskii and M. Yoshio, *Mater. Adv.*, 2024, **5**, 561.

48 M. Alaasar, S. Poppe, Q. Dong, F. Liu and C. Tschierske, *Angew. Chem., Int. Ed.*, 2017, **56**, 10801.

49 M. Alaasar, S. Poppe, Y. Cao, C. Chen, F. Liu, C. Zhu and C. Tschierske, *J. Mater. Chem. C*, 2020, **8**, 12902.

50 A. H. Schoen, NASA Technical Note TN D-5541, 1970.

51 M. Blanke, T. Neumann, M. E. G. Suburu, O. Prymak, C. Wölper, C. A. Strassert and M. Giese, *ACS Appl. Mater. Interfaces*, 2022, **14**(50), 55864.

52 J. Voskuhl and M. Giese, *Aggregate*, 2022, **3**, e124.

© 2024 The Author(s). Published by the Royal Society of Chemistry